

Controllable Self-Induced Passivation of Hybrid Lead Iodide Perovskites toward High Performance Solar Cells

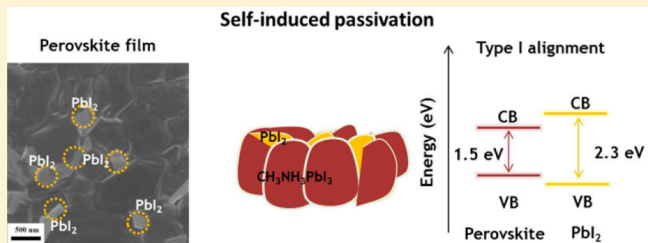
Qi Chen,^{†,‡,§} Huanping Zhou,^{*,†,‡,§} Tze-Bin Song,^{†,‡} Song Luo,^{†,‡} Ziruo Hong,[†] Hsin-Sheng Duan,^{†,‡} Letian Dou,^{†,‡} Yongsheng Liu,^{†,‡} and Yang Yang^{*,†,‡}

[†]Department of Materials Science and Engineering and [‡]California NanoSystems Institute, University of California, Los Angeles, California 90095, United States

Supporting Information

ABSTRACT: To improve the performance of the polycrystalline thin film devices, it requires a delicate control of its grain structures. As one of the most promising candidates among current thin film photovoltaic techniques, the organic/inorganic hybrid perovskites generally inherit polycrystalline nature and exhibit compositional/structural dependence in regard to their optoelectronic properties. Here, we demonstrate a controllable passivation technique for perovskite films, which enables their compositional change, and allows substantial enhancement in corresponding device performance. By releasing the organic species during annealing, PbI₂ phase is presented in perovskite grain boundaries and at the relevant interfaces. The consequent passivation effects and underlying mechanisms are investigated with complementary characterizations, including scanning electron microscopy (SEM), X-ray diffraction (XRD), time-resolved photoluminescence decay (TRPL), scanning Kelvin probe microscopy (SKPM), and ultraviolet photoemission spectroscopy (UPS). This controllable self-induced passivation technique represents an important step to understand the polycrystalline nature of hybrid perovskite thin films and contributes to the development of perovskite solar cells judiciously.

KEYWORDS: Perovskite, photovoltaics, passivation, reduced recombination, polycrystalline film



Organic/inorganic hybrid perovskite materials have recently emerged in the center of the field of photovoltaics because of their rapidly boosted power conversion efficiency (PCE) over 17% within 5 years, and their cost-effective and scalable processability.^{1–7} The investigation on perovskite materials (e.g., CH₃NH₃PbX₃, X = Cl, Br, I) has revealed its great potential for photovoltaic application, featuring with optimum band gap, high absorption coefficient, and superior ambipolar carrier transport properties.^{8–12} One typical perovskite solar cell adopts a simple planar p-i-n architecture:^{5,13} the perovskite layer is sandwiched between two electrode buffers that extract charge carriers selectively. It is of key interest to control carrier behavior such that most photogenerated carriers are able to escape out of the absorber before recombination occurs. In this regard, to minimize the energetic disorderliness (i.e., charge traps and structural defects) in the perovskites films is essential to lower carrier recombination rate and improve device performance.

In pursuit of such a planar heterojunction, numerous efforts have been focused on perovskite film formation. Various processing techniques have been documented, such as solution process,^{13–20} vacuum deposition,^{5,21} and vapor assisted solution process (VASP).²² It is suggested that the optoelectronic properties of perovskite film are closely related to the processing conditions. For example, when targeting CH₃NH₃PbI_xCl_{3-x} by codeposition of CH₃NH₃I and PbCl₂,

the precursors with nonstoichiometric (3:1) or stoichiometric ratio (1:1) lead to substantial difference on the film quality and device performance.^{23,24} Meanwhile, the kinetic/thermodynamic parameters that governs film formation are investigated either by tuning the annealing temperature, time, and ramping rate,^{13–15} or by employing different solvents or additives.^{16,17} Despite tremendous efforts in film formation, a rational guideline to process perovskite films is still less explored, due to their elusive characteristics in the context of the materials chemistry and physics. Generally, this family of perovskites are composed of inorganic framework and intercalated organic species, and their optical/electronic properties are strongly dependent on the structure and composition. Furthermore, the perovskite films inherit the polycrystalline nature with large surface area and grain boundaries (GBs). Thus, it is critically important to exploit the surface/interfaces and GBs in the perovskite films that affect the carrier behavior within the relevant heterojunction. Accordingly, a technique will be developed to achieve delicate control over the film property that promote charge generation, transportation, and collection in the solar cell ultimately.

Received: May 18, 2014

Revised: June 22, 2014

Published: June 24, 2014



Here, we use $\text{CH}_3\text{NH}_3\text{PbI}_3$ as an example to investigate the hybrid perovskite film with the emphasis on the surface and GBs, and demonstrate a controllable approach for self-induced passivation to control the carrier behavior across the corresponding heterojunction. VASP method²² is employed to construct compact and uniform $\text{CH}_3\text{NH}_3\text{PbI}_3$ films, which offers feasibility to intentionally control the incorporation of $\text{CH}_3\text{NH}_3\text{I}$ into the PbI_2 framework, as well as the release of $\text{CH}_3\text{NH}_3\text{I}$ from $\text{CH}_3\text{NH}_3\text{PbI}_3$ film. Upon thermal annealing, a compositional/structural conversion from $\text{CH}_3\text{NH}_3\text{PbI}_3$ to PbI_2 occurred mostly at the GBs of the film. It retards the carrier recombination in the corresponding planar heterojunction and improves the device performance consequently. The underlying passivation mechanism by the locally presence of PbI_2 in the $\text{CH}_3\text{NH}_3\text{PbI}_3$ film is discussed. By understanding and utilizing the polycrystalline nature of perovskite film, it is believed the passivation technique provides an effective and efficient approach to further promote perovskite solar cells.

All the devices adopted the planar heterojunction configuration of FTO/TiO₂/perovskite/spiro-OMeTAD/Au. The perovskite ($\text{CH}_3\text{NH}_3\text{PbI}_3$) thin film was fabricated via VASP,²² where the PbI_2 framework was formed first, and converted to perovskites by subsequent treatment of $\text{CH}_3\text{NH}_3\text{I}$ vapor *in situ*. The detailed device fabrication procedure is described in the methodology section. Figure 1 and Table 1

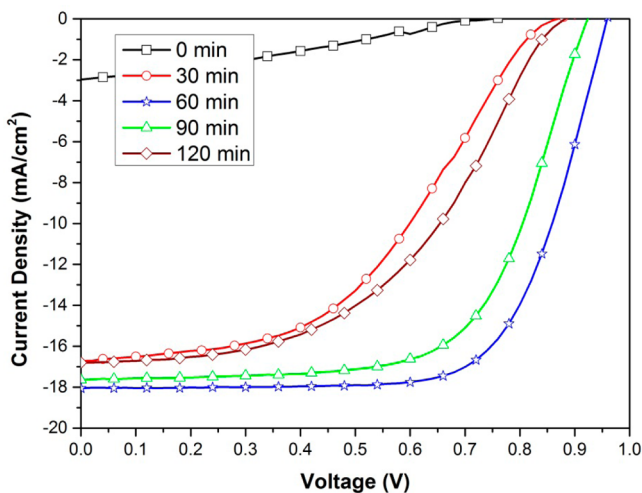


Figure 1. Current–voltage curve of the perovskite devices, where the absorbers are obtained by postannealing the $\text{CH}_3\text{NH}_3\text{PbI}_3$ film at 150 °C for different time.

Table 1. Summary of the J–V Parameters of Perovskite Devices, Where the Absorbers Are Prepared by Postannealing the $\text{CH}_3\text{NH}_3\text{PbI}_3$ Film in Different Time

annealing time	V_{oc} (V)	J_{sc} (mA/cm ²)	FF	PCE (%)
0 min	0.753	2.72	32.17	0.66
30 min	0.869	16.72	45.72	6.64
60 min	0.959	18.05	69.32	12.00
90 min	0.924	17.65	64.97	10.59
120 min	0.883	16.80	48.37	7.17

depicts the current density (J)–voltage (V) characteristic of the devices fabricated with the same film formation condition but different post annealing time at 150 °C. Without post annealing, the device showed a very low efficiency of less than 1%, with V_{OC} , J_{SC} , and FF of 0.753 V, 2.72 mA/cm², and

32.17%, respectively. The low fill factor suggests very high series resistance in the device. It is presumably due to the presence of charge traps in the film that quench the photogenerated carriers, as will be evidenced later. The PCE jumped up to 6.64% in the device enduring 30 min of annealing, with dramatic improvement in J_{SC} , V_{OC} , and FF. However, the main loss of the device is the relatively low FF of 45.72%, suggesting alleviated recombination loss but severe charge carrier accumulation to cause formation of space charge regions somewhere in the device. The optimized annealing time is 60 min, when the device achieved a PCE of 12.0%, with V_{OC} , J_{SC} , and FF of 0.959 V, 18.05 mA/cm², and 69.32%, respectively. Possibly, the improved J_{SC} is ascribed to the reduced recombination in the perovskite film, and the improved V_{OC} and FF suggests that the carrier transport layers successfully extracted carriers from the absorber due to their intimate contact and proper energy alignment. Further increasing annealing time to 120 min, however, was not favored to device performance, where V_{OC} and FF decreased severely.

The composition/morphology evolution of the perovskite film along the thermal annealing is further investigated by a series of scanning electron microscopy (SEM) and X-ray diffraction (XRD) measurement. All the films were prepared on the FTO/TiO₂ substrates to ensure the identical condition to the working device. Four representative samples with different annealing times (0, 30, 60, and 90 min) were picked up, whose XRD pattern and SEM images are shown in Figure 2, respectively. The XRD pattern (Figure 2a) clearly shows that the pristine film without annealing is composed of the pure perovskite phase with orthorhombic structure (14.09°, 28.37°, and 31.83°). $\text{CH}_3\text{NH}_3\text{I}$ phase was negligible to be detected from the annealed films because of its easy sublimation (Figure S1, Supporting Information). SEM images (Figure 2b–e) show the corresponding morphology evolution of perovskite films upon annealing. The pristine film (Figure 2b) was compact and conformal. With the time increased to 30 min, the film (Figure 2c) kept compact and uniform, but a newly formed species appeared in the adjoining grains. The species showed relatively bright contrast compared to the adjacent grains, possibly because it is less conductive and accumulates more charges. They are speculated to be PbI_2 , as indicated in the corresponding XRD pattern. The dark grains are considered to be perovskite, prevailing in the film. It corresponds to the most intensive peak in the XRD pattern, and they showed similar morphology to those exhibited in the pristine film. Further prolonging the annealing time, more grains with light contrast were observed in the GBs, which is consistent with the enhanced intensity of PbI_2 phase in the XRD pattern. We believe that $\text{CH}_3\text{NH}_3\text{PbI}_3$ decompose upon heating at 150 °C, where $\text{CH}_3\text{NH}_3\text{I}$ species escaped from the perovskite film to form the PbI_2 phase. This further indicates the weakly bonded nature between the organic and inorganic species in the hybrid perovskite. These findings, combined with our previous study that the $\text{CH}_3\text{NH}_3\text{PbI}_3$ is stable in the presence of $\text{CH}_3\text{NH}_3\text{I}$ species at moderate temperature,²² suggests a kinetically favorable reversible reaction between organic and inorganic species. The unique reversible reaction through VASP governs the amount of PbI_2 in the film that correlates to the device performance, which is further investigated below.

To bridge the enhanced device performance to the PbI_2 presence, we further employed the time-resolved photoluminescence decay (TRPL) to measure the carrier lifetime

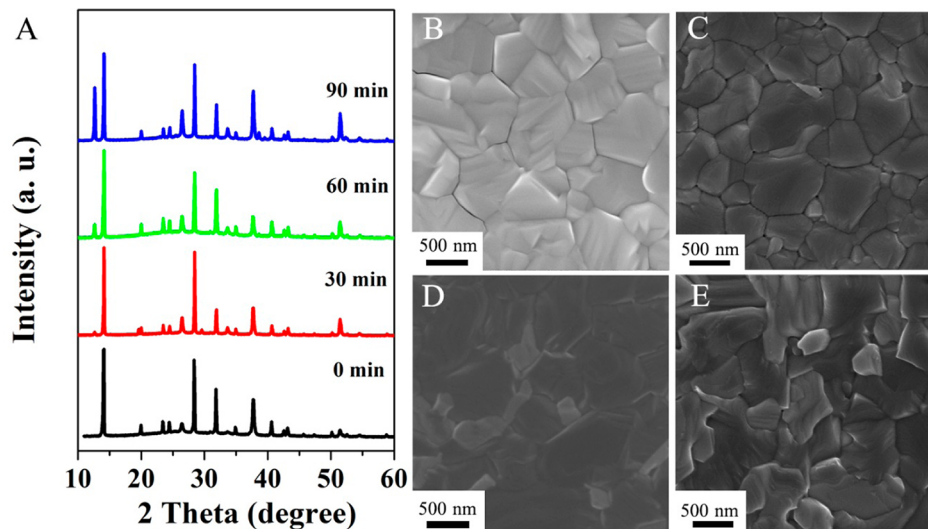


Figure 2. Time evolution characterization of the perovskite thin film, by annealing $\text{CH}_3\text{NH}_3\text{PbI}_3$ at 150°C : (a) XRD patterns of the film annealed at 0, 30, and 60, 90 min, respectively. (b–d) Top-view SEM images of different annealing time: (b) 0 min; (c) 30 min; (d) 60 min; and (e) 90 min.

in the representative perovskite films. Figure 3 shows the PL decay curves monitored at the wavelength of 775 nm, extracted

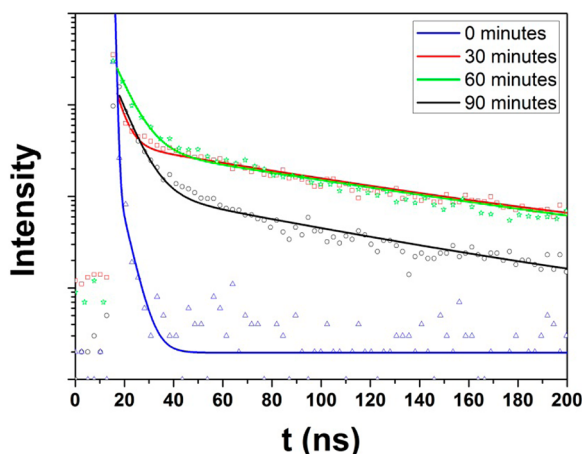


Figure 3. Photoluminescence decay curves of perovskite films prepared by postannealing the $\text{CH}_3\text{NH}_3\text{PbI}_3$ film in different time.

from the perovskite films prepared on the glass substrates. All the curves are fitted with two-component exponential decay in accordance to a previous report,²⁵ as summarized in Table 2.

Table 2. Fitting Decay Times of Perovskite Films Prepared by Postannealing the $\text{CH}_3\text{NH}_3\text{PbI}_3$ Film in Different Time

annealing time	τ_1 (ns)	τ_2 (ns)
0 min	3.65	
30 min	3.67	91
60 min	6.39	101.3
90 min	6.11	82.2

The fast decay component, τ_1 , might come from bimolecular recombination.²⁶ The long decay component τ_2 could be attributed to recombination of free carriers in the radiative channel,²⁷ which exhibit the same scale of lifetime to the previously reported PL decay in $\text{CH}_3\text{NH}_3\text{PbI}_3$ film.²⁸ In the pristine film, the fast component dominated the PL decay with

negligible slow component in the pristine film, suggesting a severe recombination occurred that leads to the extremely low photocurrent from the photovoltaic device. Upon 30 min annealing, τ_1 remains similar, but τ_2 appears to be reaching ~ 100 ns representing prolonged carrier lifetime of the film. The enhanced PL lifetime indicates the reduced recombination in the film, and it is associated with the appearance of PbI_2 phases in the $\text{CH}_3\text{NH}_3\text{PbI}_3$ film. When the annealed time prolonged from 30 to 60 min, the carrier lifetime of the film stays the same. It means that an increased amount of PbI_2 in the film does not affect the carrier recombination behavior significantly. By further prolonging the annealing time to 90 min, τ_2 dropped slightly (~ 80 ns), which may suggest a distinctive mechanism of defect chemistry when the PbI_2 phase becomes one of the major phases in the film. The carrier lifetime indicative of the recombination behavior of the film affects the device performance, as shown in Table 2. The perovskite film that experienced 1 h postannealing time leads to the best PCE. Annealing too long will degrade the perovskite film, which deteriorates the device performance by introducing a large amount of excessive PbI_2 (Figure S2, Supporting Information).

Scanning kelvin probe microscopy (SKPM) is further employed to examine the surface and GBs in the perovskite film. The SKPM has been used to determine the surface potential difference between GBs and inner grains in a thin film solar cell, which helps to reveal the band bending in the energy band diagram around the GBs. Spatial maps of topography and surface potential for the two samples (with and without annealing) are shown in Figure 4. The film without annealing exhibits a higher surface potential at the GBs than that at the bulk for around 50 mV, which is consistent with the previous observation in the mesoporous-structured perovskite solar cells.²⁹ In contrast, the surface potential at the GBs is lower than that of the bulk on the average of around 30 mV in the annealed film (60 min annealing time). The surface potential difference change is resulted from newly formed PbI_2 phases. It affects the device performance by changing the carrier behavior at the relevant interfaces to some extent as will be discussed in the following section.

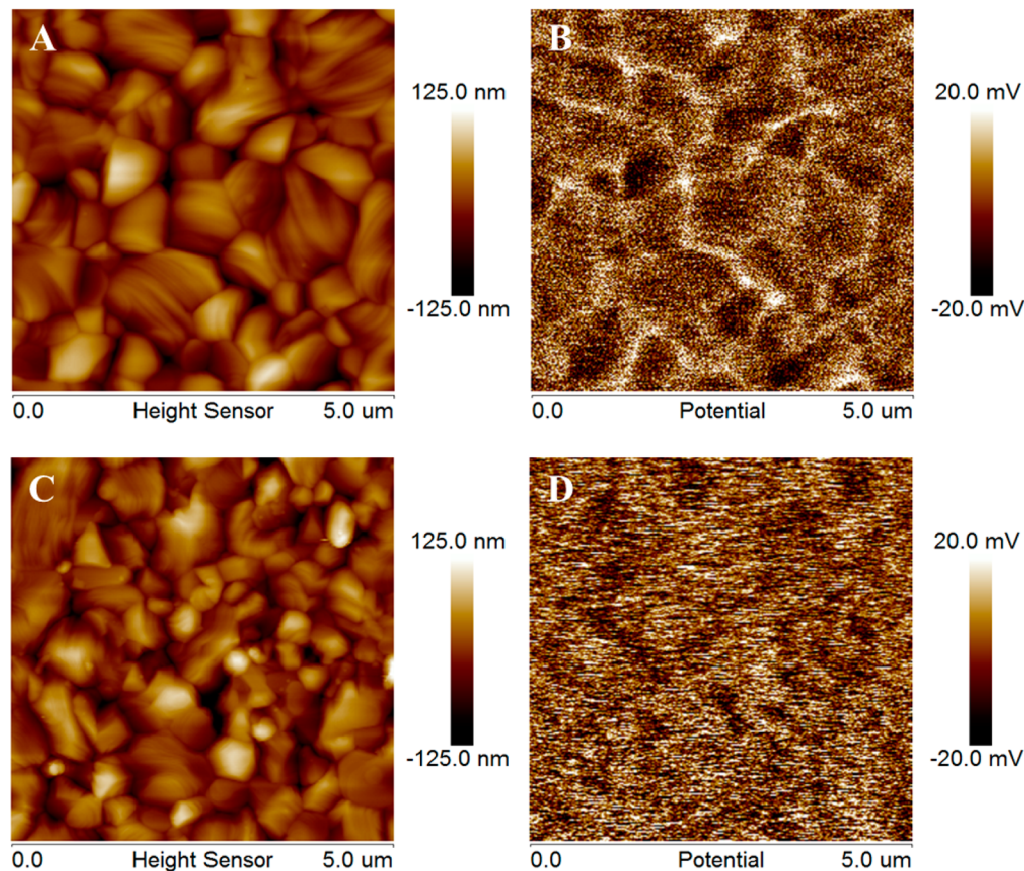
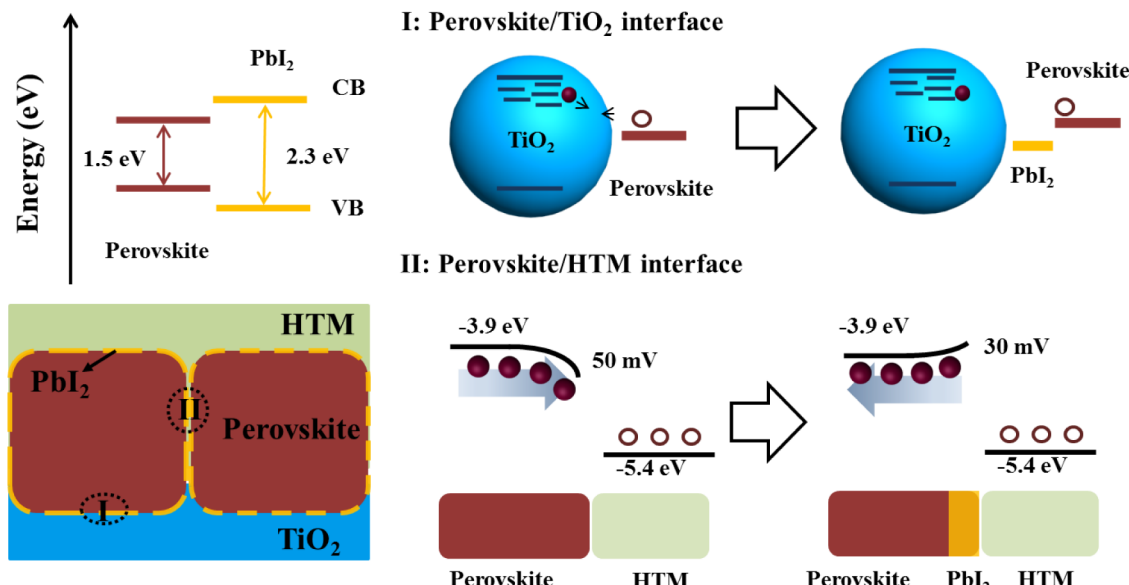


Figure 4. Two-dimensional topography spatial maps of (A) pristine perovskite film and (C) perovskite film annealed at 150 °C for 60 min. Two-dimensional surface potential spatial maps of (B) pristine perovskite film and (D) perovskite film annealed at 150 °C for 60 min.

Scheme 1. Proposed Mechanism for PbI₂ Passivation in CH₃NH₃PbI₃ Film^a



^aThe coexistence of PbI₂ and perovskite in the film shows a type I alignment of the band edge, with the band gap of 2.3 and 1.5 eV, respectively. The schematic p-i-n structure is shown in the bottom left. The interface (I) of perovskite/TiO₂ is shown on the top right; and the recombination of electron from TiO₂ and holes from perovskite is reduced by the introduction of PbI₂. The interface (II) of perovskite/HTM is described on the bottom right; the presence of PbI₂ changes the grain to grain boundary bending from downward to upward, which helps to reduce the recombination between the electrons from perovskite and holes from HTM.

The presence of PbI₂ closely correlates to the enhanced device performance. Combining the characterization results, we

speculate that the PbI₂ passivation promotes the device performance by reducing carrier recombination in the absorber

materials, as well as in the interfaces between absorber and the carrier transport layer, as summarized in Scheme 1.

First, PbI_2 greatly reduced the surface recombination in the $\text{CH}_3\text{NH}_3\text{PbI}_3$ absorber. In the pristine film, a short carrier lifetime was observed, indicating most carriers are trapped by the defects. Considering the high crystallinity nature of $\text{CH}_3\text{NH}_3\text{PbI}_3$, defects might have a large chance to occupy the sites at the surface and GBs. Upon thermal annealing, the $\text{CH}_3\text{NH}_3\text{I}$ escape from the GBs to generate a PbI_2 rich region. A stronger PL intensity and longer decay time of the $\text{CH}_3\text{NH}_3\text{PbI}_3$ film was observed as well (Figures 3 and S4, Supporting Information). We believe the reduced carrier recombination with the presence of PbI_2 in the perovskite film is related to the favored energy band alignment, as shown in Scheme 1. The conduction band minimum (CBM) and valence band maximum (VBM) for $\text{CH}_3\text{NH}_3\text{PbI}_3$ are generally reported to be 3.93 and 5.43 eV, respectively.⁶ The CBM and VBM for PbI_2 are analyzed with a combination of ultraviolet photoemission spectroscopy (UPS) (Figure S5, Supporting Information) and UV absorption, with a value of 3.45 and 5.75 eV, respectively. This type I band alignment between PbI_2 and perovskite forms energy barriers to prevent excitons from the surface defects and traps states. Thus, a carrier transport route with less nonradiative channels is presented in the film. The self-induced conversion of PbI_2 effectively passivates the grain locally, resulting in a substantially reduced carrier recombination and enhanced device performance.

It is also proposed that the PbI_2 passivation leads to the reduction of recombination at the interface of TiO_2 /perovskite. In a typical cross-section SEM image of the annealed film (60 min, Figure S6, Supporting Information), discrete PbI_2 grains are also presented at the perovskite/ TiO_2 interface. It is reported that TiO_2 exhibits predominant surface defects (Ti^{3+} sites) serving as deep electron-donating sites with energy level located at approximately 5.0 eV.³⁰ Thus, they are prone to recombine the holes in the perovskite (5.43 eV) due to energy matching. The presence of wide bandgap PbI_2 species at the interface, however, probably help to reduce the recombination probability (Scheme 1, I). The similar reduced carrier recombination has been widely used in thin film solar cell, as the interface between the p–n junction or absorber/carrier selective layer shows a relatively high recombination rate. Thus, we attributed the improved device performance partly to the decreased carrier recombination at the interface of TiO_2 /perovskite with the involvement of PbI_2 species. Because of its wide bandgap, however, PbI_2 in the interface of TiO_2 /perovskite may block the electron transportation along the device to some extent. It requires further study to delicately control the amount of PbI_2 at the interface.

Furthermore, we speculate that the passivated GBs might alleviate the barrier of charge extraction from perovskite to the hole transport layer (HTL). From SKPM results, the pristine perovskite film shows higher surface potential at GBs than that in the bulk, which is similar to the $\text{Cu}(\text{InGa})\text{Se}_2$ polycrystalline film.³¹ It generally leads to a downward bending of the energy band at the GBs, where the electrons are attracted, but holes are repelled³¹ (Scheme 1, II). In a practical device, spiro-OMeTAD easily infiltrates into the perovskite film at the GBs to extract holes from these interfaces. Because of the downward bending at the GBs of the perovskite, unfortunately, the hole extraction is retarded. After passivation, the higher surface potential at the GBs is diminished, which suppresses the barrier for hole extraction to some extent. Comparing samples with and

without annealing, the difference of the surface potential is only several tens of millivolts, which might not be large enough to result in apparent variation in J – V characteristics of the device. So it is difficult to conclude the beneficial effect of the GBs is prevailing in determining the device performance. However, it is worth noting that our results show some relevance with the simulation results on the GB property, where the typical Pb and I atoms at the GB regions do not show deep gap states.³² Although finding out the nature of the defects in the GB and grain interior is beyond the scope of current research, this different grain boundary behavior may represent a direction to develop more efficient defect passivation.

Our results are consistent with previous observation through surface photovoltage spectroscopy analysis,³³ which points out that charge separation from defect states were reduced by PbI_2 passivation. Here we bridge the film property to device performance by revealing the underlying passivation mechanism. This is also coincidence with the frequent appearance of PbI_2 (regardless of its weak intensity) in most high performance perovskite solar cells based on either $\text{CH}_3\text{NH}_3\text{PbI}_3$ or $\text{CH}_3\text{NH}_3\text{PbI}_x\text{Cl}_{3-x}$.^{4,5} Whether this tiny amount of PbI_2 is passivating the perovskite film requires careful examination; however, a relationship between the presence of PbI_2 in the film and the positive device performance is expected.

Having established that PbI_2 plays a positive role on the perovskite film in the solar cell devices, the next step is to investigate the nature of the grain interiors, grain boundaries, and surfaces of grains, and how to rationally design an effective passivation method. The self-induced passivation can be properly realized by tuning both the stoichiometric ratio between the inorganic/inorganic species, and the annealing process as well. Besides, the incorporation of extrinsic elements or ions in the perovskite film will be readily studied through dissolving the desired constituent in the precursor or post-treating the pristine film. It should be emphasized that a deeper understanding of carrier dynamics in the passivated film and the reduction of recombination through a proper passivation of the perovskite film could be critical.

In summary, we have demonstrated a general approach to effective passivation of $\text{CH}_3\text{NH}_3\text{PbI}_3$ film, with a significantly improved carrier electric property and thus device performance. It has been shown that the presence of PbI_2 species in the GBs upon thermal annealing lead to a successful passivation that control the carrier behavior along the heterojunctions. Systematical studies indicate that a proper amount of PbI_2 species in the $\text{CH}_3\text{NH}_3\text{PbI}_3$ film led to improved carrier behavior possibly due to reduced recombination in the GBs and the TiO_2 /perovskite surface. Additionally, the GB property of the perovskite film behaved differently after passivation. Future work will be focused on the nature of the grain boundary of perovskite materials to design some rational approach to passivate the film. Continuous work on reducing the recombination in perovskite solar cell will promise a real low-cost, high efficiency photovoltaic technique.

■ ASSOCIATED CONTENT

Supporting Information

Detailed experimental procedures and Figures S1 to S6. This material is available free of charge via the Internet at <http://pubs.acs.org>.

■ AUTHOR INFORMATION

Corresponding Authors

*(H.Z.) E-mail: happyzhou@ucla.edu.
*(Y.Y.) E-mail: yangy@ucla.edu.

Author Contributions

§(Q.C. and H.Z.) These authors contributed equally to this work.

Notes

The authors declare no competing financial interest.

■ ACKNOWLEDGMENTS

This work was financially supported by a grant from the National Science Foundation (grant number ECCS-1202231, Program Director Dr. Paul Werbos), Air Force Office of Scientific Research (Grant number FA9550-12-1-0074, Program Manager Dr. Charles Lee), and UCLA Internal Funds. The authors are grateful for Dr. Adam Steig's help on SKPM characterization and valuable discussion on the surface potential in perovskite thin film.

■ REFERENCES

- (1) Best Research Cell Efficiencies. http://www.nrel.gov/ncpv/images/efficiency_chart.jpg.
- (2) Kojima, A.; Teshima, K.; Shirai, Y.; Miyasaka, T. *J. Am. Chem. Soc.* **2009**, *131*, 6050–6051.
- (3) Heo, J. H.; Im, S. H.; Noh, J. H.; Mandal, T. N.; Lim, C. S.; Chang, J. A.; Lee, Y. H.; Kim, H.; Sarkar, A.; Nazeeruddin, M. K.; Grätzel, M.; Seok, S. *Nat. Photonics* **2013**, *7*, 486–491.
- (4) Burschka, J.; Pellet, N.; Moon, S. J.; Humphry-Baker, R.; Gao, P.; Nazeeruddin, M. K.; Grätzel, M. *Nature* **2013**, *499*, 316–319.
- (5) Liu, M.; Johnston, M. B.; Snaith, H. J. *Nature* **2013**, *501*, 395–398.
- (6) Kim, H. S.; Lee, C. R.; Im, J. H.; Lee, K. B.; Moehl, T.; Marchioro, A.; Moon, S. J.; Humphry-Baker, R.; Yum, J. H.; Moser, J. E.; Grätzel, M.; Park, N. G. *Sci. Rep.* **2012**, *2*, 591.
- (7) Lee, M. M.; Teuscher, J.; Miyasaka, T.; Murakami, T. N.; Snaith, H. J. *Science* **2012**, *338*, 643–647.
- (8) Snaith, H. J. *J. Phys. Chem. Lett.* **2013**, *4*, 3623–3630.
- (9) Boix, P. P.; Nonomura, K.; Mathews, N.; Mhaisalkar, S. G. *Mater. Today* **2014**, *17*, 16–23.
- (10) Kazim, S.; Nazeeruddin, M. K.; Grätzel, M.; Ahmad, S. *Angew. Chem., Int. Ed.* **2014**, *53*, 2812–2824.
- (11) Park, N.-G. *J. Phys. Chem. Lett.* **2013**, *4*, 2423–2429.
- (12) Kim, H.-S.; Im, S. H.; Park, N.-G. *J. Phys. Chem. C* **2014**, *118*, 5615–5625.
- (13) Jeng, J.-Y.; Chiang, Y. F.; Lee, M. H.; Peng, S. R.; Guo, T. F.; Chen, P.; Wen, T. C. *Adv. Mater.* **2013**, *25*, 3727–3732.
- (14) Eperon, G. E.; Burlakov, V. M.; Docampo, P.; Goriely, A.; Snaith, H. J. *Adv. Funct. Mater.* **2014**, *24*, 151–157.
- (15) Saliba, M.; Tan, K. W.; Sai, H.; Moore, D. T.; Scott, T.; Zhang, W.; Estroff, L. A.; Wiesner, U.; Snaith, H. J. *J. Phys. Chem. C* **2014**, DOI: 10.1021/jp500717w.
- (16) Conings, B.; Baeten, L.; Dobbelaere, C. D.; D'Haen, J.; Manca, J.; Boyen, H. G. *Adv. Mater.* **2014**, *26*, 2041–2046.
- (17) Liang, P.-W.; Liao, C. Y.; Chueh, C. C.; Zuo, F.; Williams, S. T.; Xin, X. K.; Lin, J.; Jen, A. K. Y. *Adv. Mater.* **2014**, *26*, 3748–3754.
- (18) Liu, D.; Kelly, T. L. *Nat. Photonics* **2014**, *8*, 133–138.
- (19) You, J.; Hong, Z.; Yang, Y.; Chen, Q.; Cai, M.; Song, T. B.; Chen, C. C.; Lu, S.; Liu, Y. S.; Zhou, H.; Yang, Y. *ACS Nano* **2014**, *8*, 1674–1680.
- (20) Eperon, G. E.; Burlakov, V. M.; Goriely, A.; Snaith, H. J. *ACS Nano* **2014**, *8*, 591–598.
- (21) Malinkiewicz, O.; Yella, A.; Lee, Y. H.; Espallargas, G. M.; Graetzel, M.; Nazeeruddin, M. K.; Bolink, H. J. *Nat. Photonics* **2014**, *8*, 128–132.
- (22) Chen, Q.; Zhou, H.; Hong, Z.; Luo, S.; Duan, H. S.; Wang, S. H.; Liu, Y. S.; Li, G.; Yang, Y. *J. Am. Chem. Soc.* **2014**, *136*, 622–625.
- (23) Stranks, S. D.; Eperon, G. E.; Grancini, G.; Menelaou, C.; Alcocer, M. J. P.; Leijtens, T.; Herz, L. M.; Petrozza, A.; Snaith, H. J. *Science* **2013**, *342*, 341–344.
- (24) Wehrenfennig, C.; Eperon, G. E.; Johnston, M. B.; Snaith, H. J.; Herz, L. M. *Adv. Mater.* **2014**, *26*, 1584–1589.
- (25) Pellet, N.; Gao, P.; Gregori, G.; Yang, T. Y.; Nazeeruddin, M. K.; Maier, J.; Grätzel, M. *Angew. Chem., Int. Ed.* **2014**, *53*, 3153–3157.
- (26) Gunawan, O.; Todorov, T. K.; Mitzi, D. B. *Appl. Phys. Lett.* **2010**, *97*, 233506.
- (27) Poncea, C. S.; Savenije, T. J.; Abdellah, M.; Zheng, K.; Yartsev, A.; Pascher, T.; Harlang, T.; Chabera, P.; Pullerits, T.; Stepanov, A.; Wolf, J. P.; Sundstrom, V. *J. Am. Chem. Soc.* **2014**, *136*, 5189–5192.
- (28) Xing, G.; Mathews, N.; Sun, S.; Lim, S. S.; Lam, Y. M.; Grätzel, M.; Mhaisalkar, S.; Sum, T. C. *Science* **2013**, *342*, 344–347.
- (29) Edri, E.; Kirmayer, S.; Henning, A.; Mukhopadhyay, S.; Gartsman, K.; Rosenwaks, Y.; Hodes, G.; Cahen, D. *Nano Lett.* **2014**, *14*, 1000–1004.
- (30) Nakamura, I.; Negishi, N.; Kutsuma, S.; Ihara, T.; Sugihara, S.; Takeuchi, K. *J. Mol. Catal. A: Chem.* **2000**, *161*, 205–212.
- (31) Li, J. B.; Chawla, V.; Clemens, B. M. *Adv. Mater.* **2012**, *24*, 720–723.
- (32) Yin, W. J.; Shi, T.; Yan, Y. *Appl. Phys. Lett.* **2014**, *104*, 063903.
- (33) Supasai, T.; Rujisamphan, N.; Ullrich, K.; Chemseddine, A.; Dittrich, T. *Appl. Phys. Lett.* **2013**, *103*, 183906.